The Aeronautical Journal (2026), 1–26
doi:10.1017/aer.2026.10251

RESEARCH ARTICLE

BEMT-based blade twist optimisation of a tiltrotor in hover using artificial bee colony algorithm

Hüseyin Pekacar[1], Gönül Güneş[1], İdil Deniz Baysaltan[1], Ayberk Çağlar[2] and Hasan Huseyin Bilgic[1,3]

[1]Aeronautical Engineering, Necmettin Erbakan University, Konya, Türkiye
[2]Aerodynamics, Turkish Aerospace Inc., Ankara, Türkiye
[3]Aviation Application and Research Center, Necmettin Erbakan University, Konya, Türkiye
Corresponding author: Hasan Huseyin Bilgic; Email: hhbilgic@erbakan.edu.tr

Received: 20 July 2026 UTC; **Revised:** 10 September 2026 UTC; **Accepted:** 15 September 2026 UTC

Keywords: ABC algorithm; Blade Element Momentum Theory (BEMT); rotor aerodynamic performance; rotor blade twist optimisation; tiltrotor rotor design

Abstract

In this study, the aerodynamic effects of rotor blade twist geometry on the hover performance of the XV-15 tiltrotor were investigated. For this purpose, the twist distribution of the XV-15 tiltrotor was optimised under hover conditions using the artificial bee colony (ABC) algorithm coupled with a Blade Element Momentum Theory (BEMT)-based numerical model validated against the NASA Ames experimental data. The blade twist was parameterised using a fifth-order continuous polynomial, whose coefficients were optimised to minimise the power coefficient while maintaining a constant thrust. The developed model was subsequently employed to evaluate the aerodynamic performance of candidate twist distributions under the prescribed hover thrust condition. In addition to the single-objective optimisation, the trade-off between aerodynamic performance and total blade twist was evaluated within a Pareto-based multi-objective optimisation framework, with total blade twist treated as a geometric design metric associated with practical blade manufacturing considerations. The best-found solution reduced the power coefficient by approximately 8.63% and increased the figure of merit (FOM) by approximately 9.45% relative to the reference geometry within the present BEMT framework. This study presents a practical optimisation approach for the aerodynamic assessment of rotor blade twist distributions under hover conditions with relatively low computational cost.

Nomenclature

ABC	Artificial Bee Colony
BEMT	Blade Element Momentum Theory
BET	Blade Element Theory
CAMRAD II	Comprehensive Analytical Model of Rotorcraft Aerodynamics and Dynamics II
CFD	Computational fluid dynamics
Coll.	Collective pitch
CPU	Central processing unit
CSD	Computational structural dynamics
DDES	Delayed detached-eddy simulation
deg	Degree
DGW	Design gross weight
EGO	Efficient global optimisation
eVTOL	Electric vertical take-off and landing
FUN3D	Fully Unstructured Navier-Stokes Three-Dimensional flow solver
HART-II	Higher Harmonic Control Aeroacoustic Rotor Test II

© The Author(s), 2026. Published by Cambridge University Press on behalf of Royal Aeronautical Society. This is an Open Access article, distributed under the terms of the Creative Commons Attribution licence (https://creativecommons.org/licenses/by/4.0/), which permits unrestricted re-use, distribution and reproduction, provided the original article is properly cited.
https://doi.org/10.1017/aer.2026.10251 Published online by Cambridge University Press

HFO	High-fidelity optimisation
HMB3	Helicopter Multi-Block 3 CFD solver
lbf	Pound-force
LFO	Low-fidelity optimisation
MOABC	Multi-Objective Artificial Bee Colony
ms	Millisecond
NASA	National Aeronautics and Space Administration
NFE	Number of function evaluations
NSGA-II	Non-dominated Sorting Genetic Algorithm II
RANS	Reynolds-averaged Navier-Stokes
RMSE	Root-mean-square error
SD	Standard deviation
SLSQP	Sequential least-squares programming
SNOPT	Sparse Nonlinear OPTimizer
UAM	Urban air mobility
UH-60A	Sikorsky UH-60A Black Hawk helicopter designation
XV-15	Bell XV-15 tiltrotor research aircraft designation

Roman symbols

a	Two-dimensional lift-curve slope used in the initial collective-pitch estimate (rad^{-1})
$C_d(r)$	Local sectional drag coefficient
C_{d0}	Zero-lift profile drag coefficient
$C_l(r)$	Local sectional lift coefficient
$C_{l\alpha}, C_{l\alpha,M}(r)$	Two-dimensional lift-curve slope and its Mach-corrected local value (rad^{-1})
C_P	Rotor power coefficient
C_T	Rotor thrust coefficient
CV_λ	Coefficient of variation of the induced-inflow ratio (%)
dC_T/dr	Sectional thrust-coefficient distribution with respect to nondimensional radius
E_λ	Area-weighted standard deviation of the induced-inflow ratio
$f(r)$	Auxiliary parameter in the Prandtl tip-loss formulation
f_1, f_2	First and second objectives: aerodynamic power coefficient and total root-to-tip blade-twist variation (- / deg)
fit_i	Fitness value of candidate solution i
$F(r)$	Prandtl tip-loss factor
FM	Figure of merit
$\bar{f}_n, f_{n,min}, f_{n,max}$	Normalised objective n and the minimum and maximum values used for its normalisation (- / native)
$J(X), J_{total}(X)$	Single-objective cost function and normalised weighted-sum objective function
k_{drag}	Coefficient of the quadratic profile-drag term
K_{trim}	Trim-loop convergence coefficient
$M(r)$	Local Mach number
M_{tip}	Rotor-tip Mach number
N	Number of radial blade elements
N_b	Number of rotor blades
N_s	Number of radial stations included in the inflow-uniformity evaluation
P_i	Onlooker-bee selection probability for candidate solution i
p_0	Dependent constant coefficient of the fifth-order relative-twist polynomial (deg)
$p_1, \ldots, p_5$	Independent coefficients of the fifth-order relative-twist polynomial (deg)
r	Nondimensional radial position: local radial coordinate divided by rotor radius
R	Rotor radius (m)
r_{local}	Dimensional local radial coordinate (m)
r_i, r_k	Nondimensional radial position at blade element or station i or k
SN	Number of food sources or candidate solutions in the ABC colony

https://doi.org/10.1017/aer.2026.10251 Published online by Cambridge University Press

$v_{i,j}, x_{i,j}, x_{k,j}$	Trial, current and comparison-candidate values of design variable j in the ABC neighbourhood search (deg)
w_1, w_2	Weight coefficients in the multi-objective scalarisation, with $w_1 + w_2 = 1$
$\boldsymbol{X}$	Vector of independent twist-polynomial coefficients p_5 through p_1 (deg)

Greek symbol

$\alpha(r)$	Local angle of attack (rad in equations; deg when reported)
α_{ZLL}	Zero-lift angle of attack (rad)
ΔA_k	Annular-area weighting represented by radial station k
$\Delta C_{d,stall}$	Increment in drag coefficient applied in the separated-flow or stall regime
Δr	Nondimensional radial increment
$\Delta\theta$	Total root-to-tip blade-twist variation (deg)
ϵ_{trim}	Thrust-coefficient residual used by the collective-pitch trim loop
$\lambda(r), \lambda_k$	Local induced-inflow ratio at radial position r or station k
λ_i, λ_{i+1}	Induced-inflow value at blade element i or successive inflow iterates, according to context
$\bar{\lambda}_A$	Area-weighted mean induced-inflow ratio
$\varphi(r)$	Local inflow angle (rad)
$\varphi_{i,j}$	Uniformly distributed ABC perturbation coefficient for solution i and variable j, in $[-1, 1]$
π	Circular constant
$\sigma(r), \sigma_i$	Local rotor solidity
$\theta(r)$	Local blade pitch angle (rad in equations; deg when reported)
$\theta_{0,init}$	Initial collective-pitch estimate (rad)
θ_{root}	Blade-root angle; used for the trim pitch setting and for the reported root twist angle (rad in equations; deg when reported)
θ_{tip}	Blade-tip twist angle (deg)
θ_{tw}	Blade-twist term used in the initial collective-pitch estimate (rad)
$\theta_{twist}(r)$	Fifth-order relative-twist distribution (deg)

Subscripts

0	Zero-lift or constant/base term, according to the parent symbol
1, 2	First and second objective or associated weighting coefficient
A	Area-weighted quantity
α	Slope or derivative with respect to angle of attack
b	Blade
best	Best-found feasible solution
d	Drag
drag	Quadratic drag-rise model
i	Current iteration, blade element, or candidate-solution index, according to context
i + 1	Next iteration
init	Initial estimate
j	Design-variable index
k	Radial-station index or randomly selected ABC candidate, according to context
l	Lift
local	Dimensional local radial coordinate
M	Mach-corrected quantity
max	Maximum value
min	Minimum value
n	Objective or summation index
new	Updated iteration value
old	Previous iteration value
P	Power
ref	Reference geometry or experimental value
root	Blade-root location or root-pitch setting

https://doi.org/10.1017/aer.2026.10251 Published online by Cambridge University Press

s, S	Radial stations
stall	Separated-flow or stall increment
T	Thrust
target	Prescribed target value
tip	Blade-tip location
trim	Collective-pitch trim loop
tw	Blade-twist term in the initial collective estimate
twist	Relative blade-twist distribution
ZLL	Zero-lift line
λ	Statistic associated with the induced-inflow ratio

1.0 Introduction

Rotor blade twist optimisation has long been regarded as an important problem in the aerodynamic design of rotary-wing aircraft. In conventional rotor design, linear or low-degree-of-freedom parametric twist distributions are widely used because of their geometric simplicity and the limited number of design variables they require [1, 2]. However, local velocity, inflow and sectional aerodynamic loading vary substantially along the rotor span; therefore, a single constant twist gradient may not simultaneously provide aerodynamically favourable loading conditions over the entire span. This consideration makes the investigation of more flexible spanwise twist distributions particularly relevant for rotors of tiltrotor aircraft such as the XV-15 operating at relatively high tip Mach numbers [2, 4].

Computational methods with different levels of fidelity have been employed in optimisation studies aimed at improving the aerodynamic performance of rotor blades. High-fidelity computational fluid dynamics (CFD)-based solvers can represent complex three-dimensional rotor-flow structures in greater detail, but impose substantial computational cost when large design spaces require repeated evaluation of many candidate geometries [3]. In contrast, Blade Element Momentum Theory (BEMT)-based models provide a computationally efficient alternative, particularly for rapid and repeated exploration of the design space [4, 5].

The selection of the optimisation algorithm is also an important consideration in rotor-design problems. Because geometric design spaces may be nonlinear, and aerodynamic evaluations do not always provide derivative information directly, population-based and derivative-free metaheuristic algorithms have been used alongside gradient-based methods in rotor optimisation studies [6, 7]. The artificial bee colony (ABC) algorithm developed by Karaboga employs a population-based search mechanism based on employed, onlooker and scout bee phases [8]. Owing to its relatively small number of algorithmic control parameters and its ability to perform derivative-free design-space exploration, ABC was selected in the present study to optimise the coefficients defining the polynomial twist distribution [9].

Within this broader methodological context, recent rotor and proprotor optimisation studies show that the design problem has broadened substantially in terms of aerodynamic-model fidelity, design variables and operating conditions. Current approaches range from computationally efficient blade-element/BEMT-based models to high-fidelity CFD/ computational structural dynamics (CSD) and multi-fidelity frameworks. Likewise, blade twist is frequently considered together with chord, aerofoil distribution, collective pitch, rotational speed or other geometric variables, while optimisation problems range from single-point hover designs to multi-regime formulations that include hover, forward flight, transition and cruise [19, 21–24, 27–30]. Within this broader literature, selected recent studies that are directly useful for comparison with the present work and that represent different levels of model fidelity, operating regimes, geometric design spaces and optimisation approaches are summarised in Table 1.

Comparisons in Table 1 show that key methodological elements employed in the present study – prescribed-thrust hover optimisation, smooth or polynomial twist parameterisation and population-based optimisation – have established precedents in the literature [21, 22, 29, 30]. However, a substantial portion of recent work considers twist together with other blade-design variables and/or across multiple operating regimes [21–24, 27–30]. Accordingly, the distinguishing feature of the present study is not any

https://doi.org/10.1017/aer.2026.10251 Published online by Cambridge University Press

https://doi.org/10.1017/aer.2026.10251 Published online by Cambridge University Press

Table 1. *Comparison of representative recent rotor/proprotor blade optimisation studies*

Feature	Wilke et al. [21]	Wang et al. [22]	Thurman and Wang [29]	Woodgate and Barakos [30]	This study
Rotor/Aircraft configuration	HART-II helicopter rotor	Tiltrotor	Full-scale UAM proprotor	Conventional helicopter research rotor	XV-15 tiltrotor
Operating condition(s)	Hover	Hover + tilted forward flight + high-speed cruise	Hover + cruise	Hover followed by forward flight	Hover
Aerodynamic model/Solver	Low-fidelity BET/BEMT or finite-state + CFD	BEMT + DDES verification	CAMRAD II → FUN3D multifidelity	HMB3 CFD/CSD aeroelastic framework	BEMT
Optimisation method	Surrogate-based EGO/Kriging framework	NSGA-II	Differential Evolution (LFO) + adjoint/SNOPT (HFO)	SLSQP with discrete-adjoint gradients	Artificial bee colony (ABC)
Design variables	Twist + chord-related variables	Aerofoil selection + chord + twist	LFO: collective + twist + chord; HFO: + camber + thickness	Twist + chord + sweep + anhedral	Twist only
Twist treatment/ Representation	Cubic-spline Δ-twist on baseline linear twist	Spanwise twist-angle design variables	Five spanwise control points + cubic spline in LFO	Seven-coefficient Bernstein-polynomial twist	Fifth-order continuous relative-twist polynomial (five independent coefficients)
Loading/Operating constraint	Set thrust; collective-pitch trim	Specified multi-regime operating conditions	Target disk loading in hover/cruise; trim/verification	Constrained C_T in hover	Prescribed nominal-DGW C_T; collective-pitch trim
Optimisation formulation/Objective(s)	Maximise FM at prescribed thrust (equivalent to minimising required power)	Multi-condition aerodynamic-efficiency optimisation	Multipoint hover/cruise efficiency optimisation	Hover power minimisation; sequential forward-flight optimisation	C_P minimisation at prescribed C_T; aerodynamic-efficiency / total-twist trade-off

individual methodological ingredient, but their combination within a controlled XV-15 hover problem formulated specifically to isolate the effect of spanwise twist redistribution.

Recent studies not included in Table 1 further support the multi-variable and multi-regime trend. Zeng et al. [19] considered blade twist together with other rotor-design variables in hover and cruise; Shahjahan et al. [23] performed a multivariable optimisation of tilt-wing electric vertical takeoff and landing aircraft (eVTOL) proprotors spanning cruise, hover, and transition; and Ding et al. [24] developed a multi-objective framework for high-altitude proprotor design with combined hover and cruise objectives.

A particularly relevant recent comparison for the XV-15 is provided by Kang et al. [26]. Using high-fidelity Reynolds-average Navier-Stokes (RANS) calculations for an XV-15 proprotor equipped with optimised aerofoils, the authors compared the baseline geometry with three modified overall-twist cases referenced to $0.75R$. In Kang et al. [26], however, the complete spanwise twist curve was not searched by an optimisation algorithm within a continuous design space; instead, three prescribed modified-twist cases were evaluated parametrically against the baseline geometry. In contrast, the present study represents the entire spanwise twist distribution using a fifth-order continuous polynomial with five independent coefficients, which are optimised directly by the ABC algorithm. Kang et al. [26] therefore provide an important recent assessment of the influence of twist magnitude on the same XV-15 configuration, while remaining methodologically distinct from the present twist-only stochastic approach in which the full spanwise twist distribution is optimised through a continuous polynomial parameterisation.

The broader rotor-optimisation literature also includes complementary methodological approaches. Lim et al. [20] targeted reductions in hover and forward-flight power for the UH-60A but optimised outboard aerofoil-shape parameters rather than blade twist, whereas Sancak [25] examined different twist distributions using BEMT-based parametric analyses without employing a formal optimisation algorithm. Dayhoum et al. [27] optimised chord and twist jointly using a genetic algorithm (GA), while Park et al. [28] considered twist and chord within variable- and high-fidelity aerodynamic/structural frameworks for hover and forward-flight objectives. Although older, Gadekar et al. [31] provide a directly relevant methodological precedent by parameterising both chord and twist distributions with fifth-order polynomial functions and performing blade-element/BEMT-based hover power-loading optimisation. Thus, fifth-order polynomial twist representation is not, by itself, the distinguishing feature of the present work; the distinction lies in the design problem in which the parameterisation is used and in the other design variables deliberately held fixed.

Within this literature context, the present work is formulated as a controlled twist-only design problem intended to isolate the modelled aerodynamic effect of spanwise twist redistribution for the XV-15 rotor at the nominal design gross weight (DGW) hover condition. The chord distribution, aerofoil definition and rotor speed are held fixed, while only the twist geometry is varied using a fifth-order continuous relative-twist polynomial referenced at $0.75R$ and defined by five independent coefficients. This restricted formulation provides a more controlled basis for relating the modelled performance changes to spanwise twist redistribution from a geometric-design perspective.

The focused design problem is solved at the prescribed isolated-rotor hover thrust corresponding to the nominal DGW condition. The BEMT model used within the optimisation loop is benchmarked against NASA Ames XV-15 hover data, and in the first stage the ABC algorithm minimises C_P at prescribed C_T. Stochastic repeatability is assessed through 30 independent optimisation runs, so that the best-found solution is characterised across different random initialisations rather than from a single stochastic realisation.

In the second stage, the trade-off between aerodynamic performance and total blade twist is examined within a separate multi-objective design analysis to evaluate the aerodynamic consequences of lower total-twist levels. Studies on composite blade manufacturing have shown that root-to-tip twist and local surface curvature can distort fibre paths during draping, that local fibre-steering geometry can contribute to manufacturing defects and that blade-surface geometry directly influences mould design, tolerancing and demoulding operations [32–34]. These studies demonstrate that blade twist geometry is a relevant

https://doi.org/10.1017/aer.2026.10251 Published online by Cambridge University Press

geometric consideration in composite blade manufacturing. Accordingly, total blade twist is retained in the second stage as a geometric design metric associated with manufacturing considerations, and the aerodynamic trade-off associated with reducing this quantity is quantified. Total blade twist is not, however, interpreted here as a direct measure of manufacturability.

Within this framework, the present study complements recent multi-variable and multi-regime optimisation frameworks with a focused XV-15 hover assessment. It provides a bounded and quantitative engineering evaluation of the modelled performance potential attributable to spanwise twist redistribution alone, the stochastic repeatability of the optimisation, and the aerodynamic-performance/overall-twist-demand trade-off at the nominal DGW hover condition.

2.0 Mathematical model and computational methodology

The computational procedure followed in the study is summarised in Figure 1. First, the reference operating conditions for the XV-15 rotor were defined and then the BEMT-based aerodynamic model was developed. The model was validated against NASA Ames experimental data and subsequently employed for the blade twist optimisation [10]. Using the validated model, the aerodynamic performance of different twist distributions was evaluated while maintaining the prescribed target thrust.

Each candidate blade twist distribution was parameterised using a fifth-order polynomial and evaluated with the BEMT solver. For each candidate, the induced inflow, sectional aerodynamic loads, thrust coefficient and power coefficient were computed. The trim condition and geometric feasibility were then checked. Candidates failing to satisfy the trim-convergence or geometric-feasibility requirements were handled through penalty terms incorporated into the objective function.

The optimisation loop proceeded by updating the candidate solutions using the ABC algorithm and continued until the prescribed objective-function evaluation budget was reached. For the single-objective optimisation, 30 independent runs were performed, each with a maximum budget of 10,000 objective-function evaluations, and the solution with the lowest final power coefficient among the feasible solutions satisfying the prescribed thrust condition was selected as the best-found solution. In the multi-objective optimisation, the power coefficient and total blade twist were optimised simultaneously to investigate the trade-off between aerodynamic performance and total blade twist.

2.1 Blade Element Momentum Theory (BEMT) and tip loss model

The aerodynamic coefficients of the rotor in hover were predicted using BEMT. In this approach, momentum theory was employed to determine the induced inflow, while blade element theory was used to evaluate the two-dimensional aerodynamic characteristics at each radial blade section. The rotor disk was discretised into a finite number of radial elements, and the local aerodynamic quantities were computed iteratively for each element. The overall thrust and power coefficients were then obtained by integrating the sectional aerodynamic forces along the blade span [2, 3, 11].

2.1.1 Induced inflow and Prandtl tip loss interaction

The induced inflow ratio (λ), which varies along the rotor radius, is coupled with the Prandtl tip-loss factor (F) which accounts for the reduction of vortex-induced effects near the blade tip [2]. This condition ensures that the lift generated by the rotor blades approaches zero toward the tip region and is typically solved iteratively. In the present formulation, the momentum balance is applied locally at each annular radial station of the rotor disk. Accordingly, the induced inflow ratio is evaluated as a radially varying local quantity $\lambda(r)$, rather than by prescribing a single uniform inflow value over the rotor disk. The non-dimensional induced inflow ratio at each radial station is given in Equation (1):

$$\lambda(r) = \frac{\sigma(r)\, C_{l_{\alpha,M}}(r)}{16F(r)} \left(\sqrt{1 + \frac{32F(r)}{\sigma(r)\, C_{l_{\alpha,M}}(r)} \theta(r)\, r} - 1 \right) \tag{1}$$

https://doi.org/10.1017/aer.2026.10251 Published online by Cambridge University Press

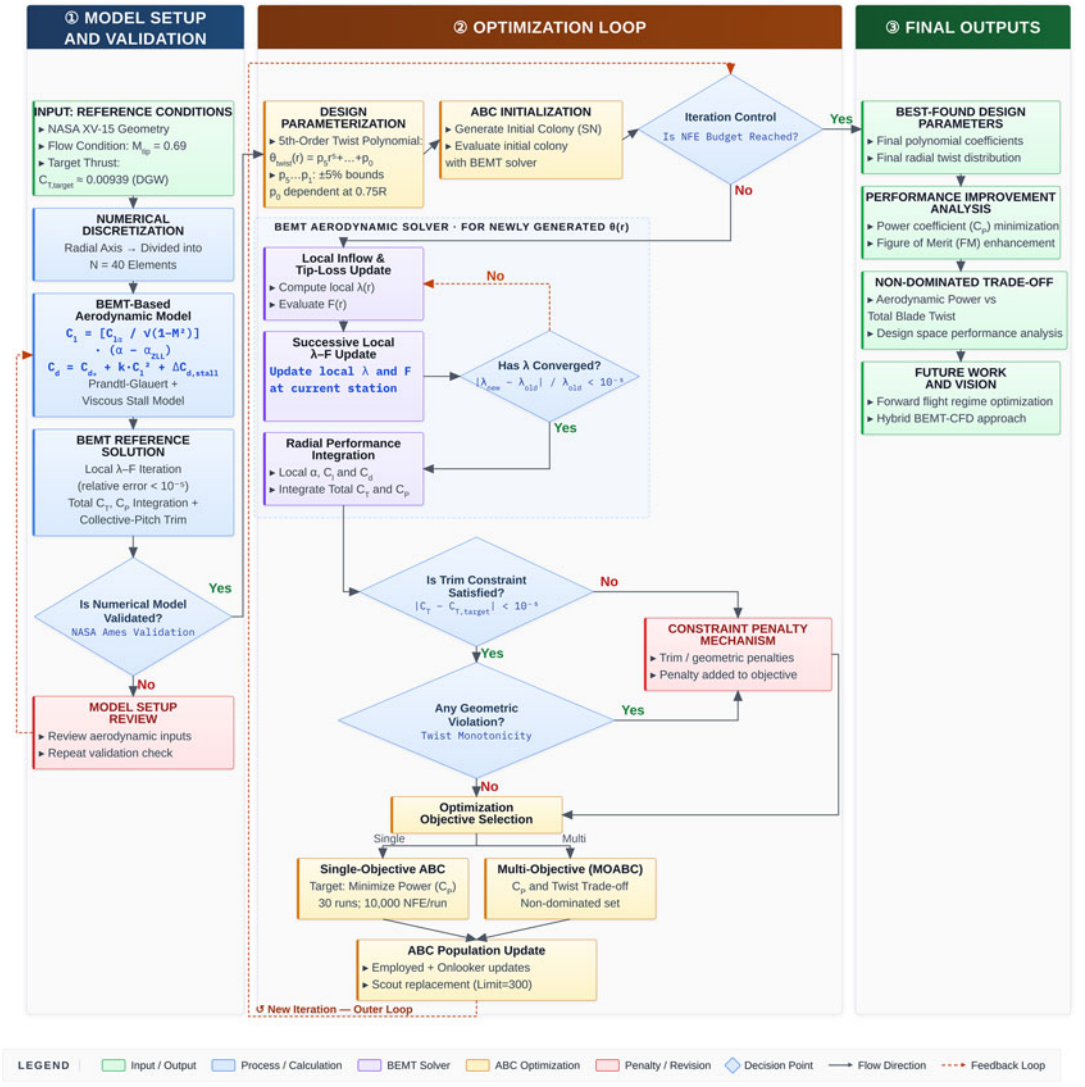


Figure 1. *Computational methodology and optimisation flowchart.*

The tip loss factor $F(r)$ in this equation is calculated using the Prandtl model, as given in Equations (2) and (3), depending on the radial position and the instantaneous induced inflow ratio:

$$f(r) = \frac{N_b}{2}\left(\frac{1-r}{\lambda\,(r)}\right) \tag{2}$$

$$F(r) = \frac{2}{\pi}\arccos(\exp(-f\,(r))) \tag{3}$$

In this approach, Equations (1) and (3) form a coupled local system through the induced inflow ratio $\lambda(r)$ and the Prandtl tip-loss factor, $F(r)$. These two quantities are updated successively at each radial station until the relative change between two successive values of λ satisfies the convergence tolerance defined in Equation (4). The converged local solution is then used for the corresponding blade element before the calculation proceeds to the next radial station.

$$\frac{|\lambda_{i+1} - \lambda_i|}{\lambda_i} < 10^{-5} \tag{4}$$

https://doi.org/10.1017/aer.2026.10251 Published online by Cambridge University Press

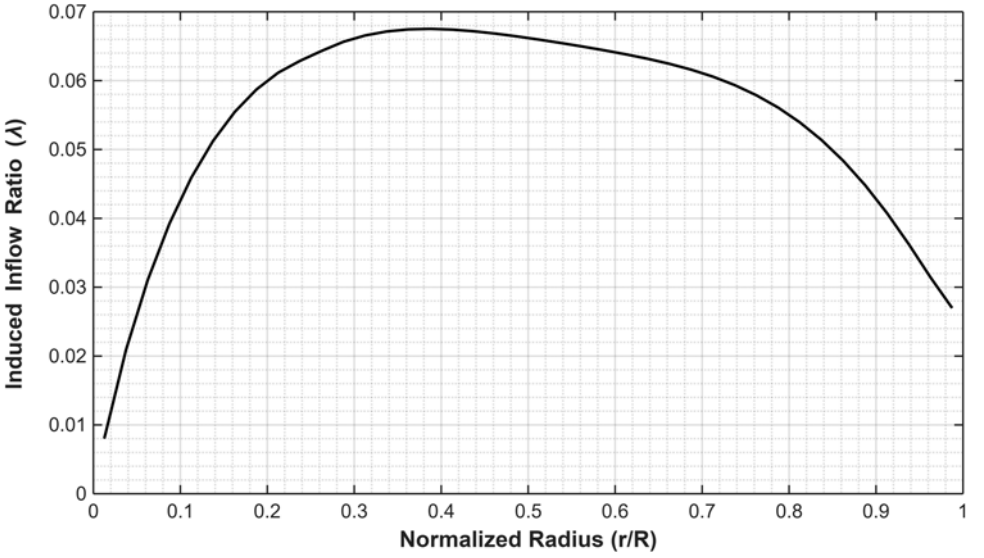


Figure 2. *Radial distribution of induced inflow (8 degrees).*

The induced inflow ratio distribution obtained from calculations, varying along the blades as a function of the non-dimensional radius (r/R), is shown in Figure 2.

2.1.2 Kinematic relations, compressibility effects, and viscous separation constraints

In BEMT analysis, the local angle-of-attack (α) on the blade element is defined as the difference between the local blade pitch angle (θ) and the inflow angle (ϕ) induced by rotor inflow [2, 3]. Under the small-angle assumption, the inflow angle and the effective angle-of-attack are given by Equations (5) and (6), respectively:

$$\phi\,(r) = \frac{\lambda\,(r)}{r} \tag{5}$$

$$\alpha\,(r) = \theta\,(r) - \phi\,(r) \tag{6}$$

Due to the design characteristics of the XV-15 aircraft, the high rotor tip Mach number ($M_{tip} = 0.69$) makes compressibility significant at the outer radial stations. To model this variation in lift characteristics, the two-dimensional linear lift curve slope (C_{l_α}) was corrected using Equation (7) as a function of the local Mach number $M(r)$ in accordance with the Prandtl-Glauert approach [12].

$$C_{l_{\alpha,M}}\,(r) = \frac{C_{l_\alpha}}{\sqrt{1 - M\,(r)^2}} \tag{7}$$

Using the corrected aerodynamic slope, the local lift coefficient (C_l) at each radial station was calculated using Equation (8), with reference to the zero-lift angle-of-attack (α_{ZLL}):

$$C_l\,(r) = C_{l_{\alpha,M}}\,(r)\,(\alpha\,(r) - \alpha_{ZLL}) \tag{8}$$

After the local lift coefficient is obtained, the profile drag coefficient of the blade element is evaluated. At high angles of attack, a rapid increase in drag is observed due to flow separation over the aerofoil [12]. The high geometric twist angles near the root region of the XV-15 rotor increase the likelihood of viscous separation in hover conditions. To numerically represent this aerodynamic behaviour, it is assumed that the aerofoil enters the stall regime if the local lift coefficient exceeds the limits of the linear attached-flow region ($-0.8 \leq C_l \leq 1.2$) [2]. Accordingly, the local drag coefficient was calculated

https://doi.org/10.1017/aer.2026.10251 Published online by Cambridge University Press

using an empirical viscous separation model formulated by Equation (9):

$$C_d(r) = \begin{cases} C_{d_0} + k_{drag} C_l(r)^2, & -0.8 \le C_l(r) \le 1.2 \\ C_{d_0} + k_{drag} C_l(r)^2 + \Delta C_{d,stall} & other\ case \end{cases} \tag{9}$$

In this equation, C_{d0} denotes the profile drag at zero lift, k_{drag} is the drag rise coefficient, and $\Delta C_{d,stall}$ represents the abrupt increase in viscous drag due to flow separation.

2.1.3 Numerical trim and performance integration

In the final stage of the BEMT analysis, the differential forces calculated on each radial element (r_k) were numerically integrated along the blade to determine the total rotor performance. The total thrust coefficient and power coefficient of the rotor were numerically summed over the step interval $\Delta(r)$ between the radial stations using Equations (10) and (11), respectively [2].

$$C_T = \sum_{k=1}^{N} \frac{1}{2} \sigma(r_k) C_l(r_k) r_k^2 \Delta r \tag{10}$$

$$C_P = \sum_{k=1}^{N} \frac{1}{2} \sigma(r_k) (C_l(r_k) \lambda(r_k) + C_d(r_k) r_k) r_k^2 \Delta r \tag{11}$$

In this study, to ensure sufficient numerical accuracy in the first stage, the radial domain was discretised into $N = 40$ equal elements ($\Delta r = 1/40$).

For the nominal DGW hover condition of the XV-15, the target thrust coefficient was set to ($C_{T,target} = 0.00939$). This value corresponds to an isolated-rotor approximation in which the 13,000-lbf DGW [18] is equally shared between the two rotors, while wing/airframe download and rotor–airframe interactions are neglected. For each candidate twist distribution, the collective-pitch setting, denoted by θ_{root} in the trim formulation, was adjusted to satisfy this thrust requirement. For this purpose, the initial collective pitch angle was estimated using momentum theory (Equation (12)), and a trim loop was implemented and updated at each iteration. The residual error between the computed and target thrust ($\epsilon_{trim} = C_{T,target} - C_T$) was evaluated, and the collective-pitch setting was updated using Equation (13):

$$\theta_{0_{init}} = \frac{6C_T}{\sigma a} + \frac{3}{2}\sqrt{\frac{C_T}{2}} - \frac{3}{4}\theta_{tw} \tag{12}$$

$$\theta_{root,i+1} = \theta_{root,i} + K_{trim}(C_{T,target} - C_T) \tag{13}$$

In Equation (13), K_{trim} represents the convergence coefficient ($K_{trim} = 2.5$). The trim loop was continued until the error fell below the tolerance of 10^{-5} or the maximum limit of 200 iterations was reached. This approach ensures that the power consumptions of all investigated aerodynamic designs are evaluated in a consistent and comparable manner under conditions where they perform the same lifting task. To verify the physical consistency of the model and boundary conditions, the radial thrust distribution obtained for $\theta_{root} = 8^\circ$ is presented in Figure 3.

The distribution profile shows that the aerodynamic load is concentrated in the outer region due to the increasing dynamic pressure and decreases at the tip boundary ($r \to R$) in accordance with physical expectations due to the Prandtl tip loss effect [2].

2.2 Numerical solution and grid independence

In the developed BEMT model, the total thrust and power coefficients were obtained by numerically integrating the differential aerodynamic forces on the blade. For this purpose, the rotor disk was discretised into a finite number of radial elements. A low number of elements increases discretisation error, whereas excessively high numbers significantly increase computational cost, particularly in optimisation loops. Therefore, a grid independence study was performed to determine an appropriate number of radial elements.

https://doi.org/10.1017/aer.2026.10251 Published online by Cambridge University Press

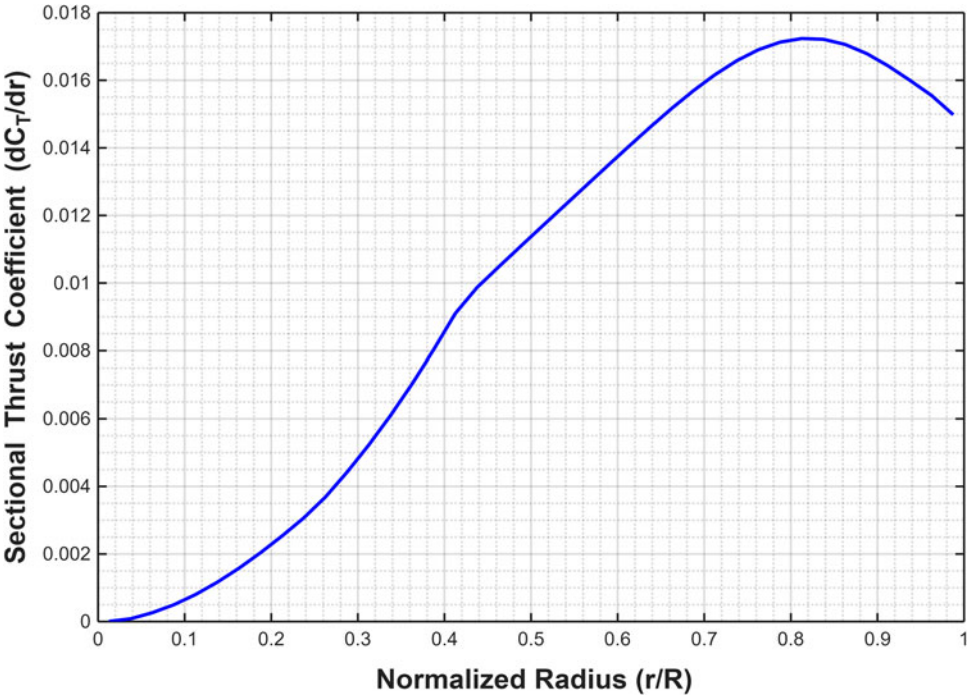


Figure 3. *Radial distribution of thrust coefficient (8 degrees).*

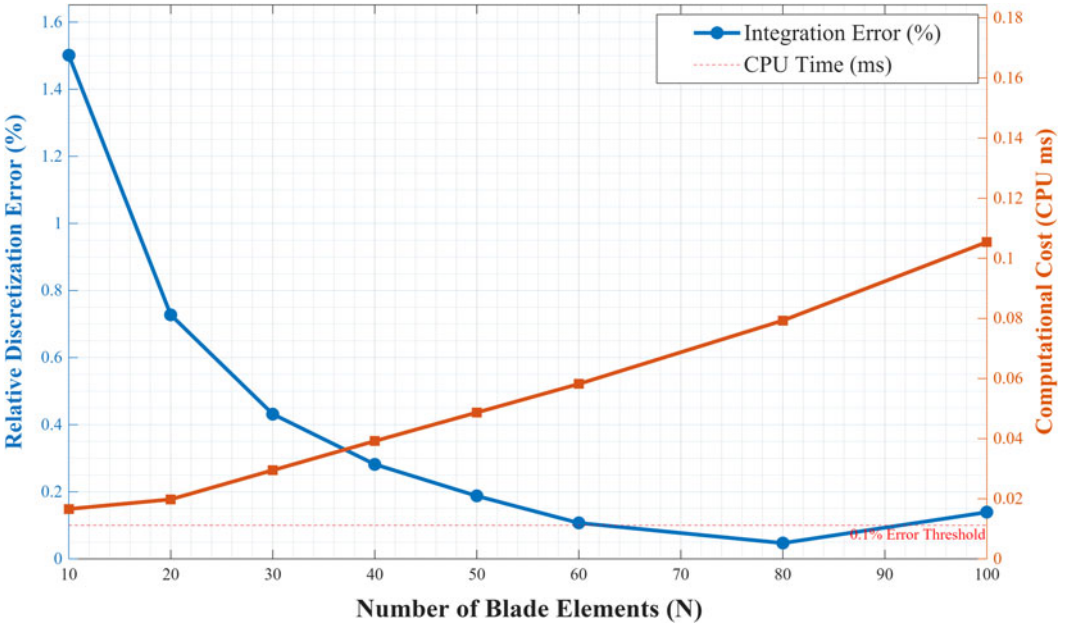


Figure 4. *Grid independence and computational cost analysis.*

The grid independence analysis performed for the hover condition ($\theta_{root} = 5°$) of the XV-15 rotor is presented in Figure 4. In this study, the number of radial elements was varied between $N = 10$ and $N = 100$. The thrust values predicted by the model were compared with a high-resolution reference solution ($N = 150$), and the relative discretisation error was calculated.

https://doi.org/10.1017/aer.2026.10251 Published online by Cambridge University Press

Table 2. *BEMT model validation (comparison with NASA XV-15)*

Coll.	CT	CT (Ref)	CT error (%)	CP	CP (Ref)	CP error (%)	FM	FM (Ref)	FM error (%)
1°	0.00482	0.00473	+ 1.8	0.00039	0.00038	+ 1.9	0.6076	0.6025	+ 0.8%
3°	0.00624	0.00641	−2.6	0.00047	0.00052	−10.7	0.7444	0.6957	+ 7.0
5°	0.00750	0.00815	−7.9	0.00062	0.00070	−12.4	0.7461	0.7398	+ 0.8
8°	0.00987	0.01096	−9.9	0.00093	0.00108	−14.0	0.7494	0.7540	−0.6
10°	0.01168	0.01301	−10.3	0.00119	0.00143	−16.6	0.7501	0.7357	+ 2.0
11°	0.01260	0.01398	−9.9	0.00134	0.00161	−17.1	0.7465	0.7236	+ 3.2

The results show discretisation error is significant for $N < 30$ range. When the number of elements reaches $N = 40$, the relative error decreases to approximately 0.3 %. Beyond this value, further refinement yields only marginal improvements in the solution. Increasing the number of elements beyond $N = 40$ does not provide a significant gain in accuracy, while it increases computational cost. Therefore, $N = 40$ was selected for all subsequent numerical analyses and optimisation studies.

2.3 Model validation: comparison with NASA experimental data

The XV-15 tiltrotor experimental data published by NASA's Ames Research Center were used as a reference for the validation of the numerical model. The comparison was performed using the Run 14 data set, which consists of isolated rotor hover tests in which rotor–fuselage interactions are neglected. Consistent with the experimental conditions, the analysis was conducted at standard sea-level conditions where the tip Mach number is $M_{tip} = 0.69$ [10].

To evaluate the response of the numerical model under different aerodynamic loading conditions, the root collective angle was varied in the range of 1° to 11°. The resulting thrust coefficient, power coefficient and figure of merit (FOM) values were compared with the experimental data and are presented in Table 2.

The results in Table 2 show that the numerical model captures the overall aerodynamic trend. The error levels remain limited at low collective angles ($\theta_{root} \leq 3°$). In contrast, under medium and high lift conditions (5°–11°), the BEMT model underpredicts the thrust by approximately 7–10% compared to the experimental data. The power coefficient is also underpredicted by approximately 12–17%.

The nominal DGW hover target used in the optimisation ($C_{T,target} = 0.00939$) lies within the loading range examined in the validation and is close to the BEMT result obtained at 8°collective ($C_T = 0.00987$).

These deviations are primarily attributed to the two-dimensional aerodynamic formulation of the BEMT approach. In particular, three-dimensional flow separation at the rotor root region, tip vortex effects and increased induced drag at high angles of attack cannot be fully captured. As a result, the model predicts lower C_P and C_T values at medium and high collective angles relative to the experiments.

When the FOM is considered separately, the discrepancy between the numerical model and the experimental data is smaller compared to the C_P and C_T results.

The thrust and power coefficient graphs shown in Figure 5 indicate a systematic underprediction tendency, particularly at medium and high collective angles. In contrast, the FM curve follows the experimental trend more closely over the same range.

Due to the relationship $FM \propto \frac{C_T^{1.5}}{C_P}$, the error trends in C_T and C_P are partially compensated in the FOM calculation. As a result, the deviation in FOM values remains more limited compared to those of the thrust and power coefficients. Within the medium-to-high loading range examined in the validation $5° - 11°$, the numerical FOM predictions deviate from the experimental data by approximately 0.6–3.2%.

https://doi.org/10.1017/aer.2026.10251 Published online by Cambridge University Press

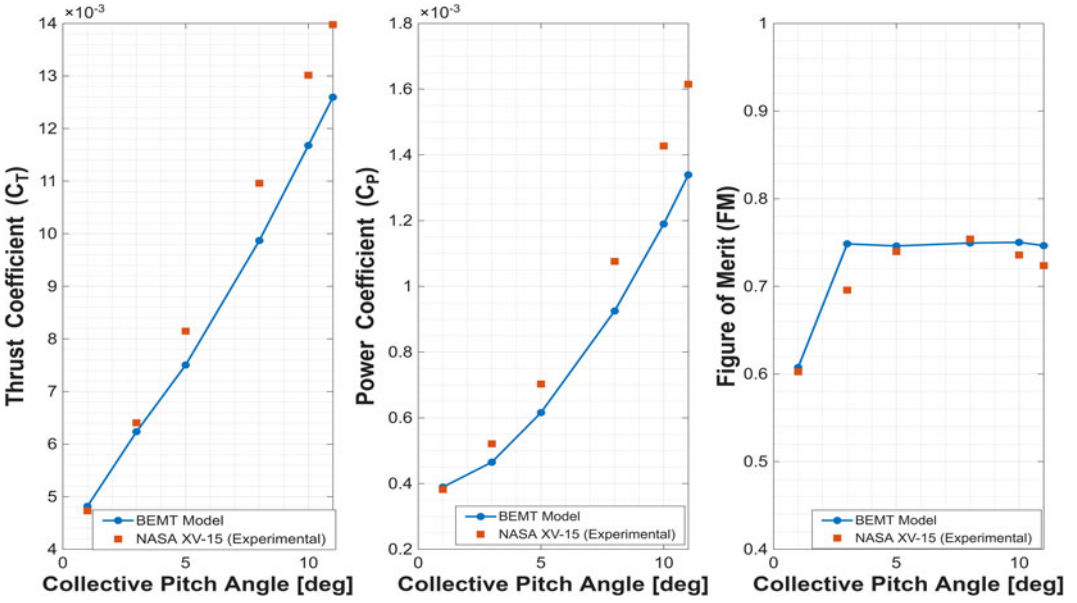


Figure 5. *Thrust, power and FOM validation plots.*

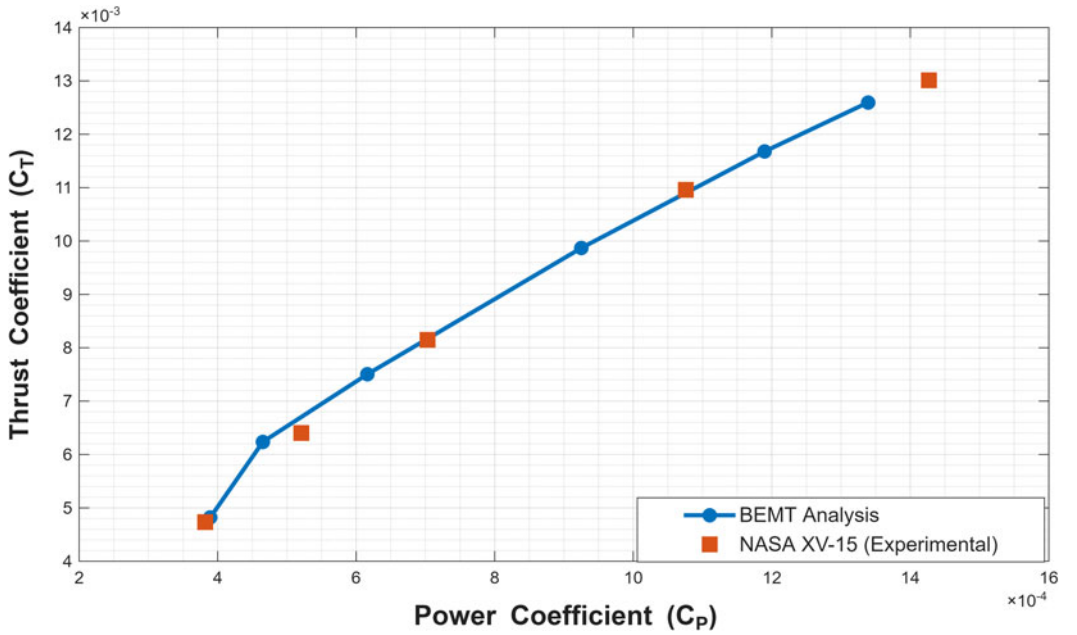


Figure 6. *Thrust and power coefficient comparison analysis.*

The $C_T - C_P$ relationship shown in Figure 6 indicates that the model captures the general trend between thrust and power coefficients. Although a relative underprediction is observed in both C_T and C_P at medium and high collective angles, the effect of these deviations remains limited in the FOM calculation. These validation results support the use of the BEMT solver for comparative design evaluations within the present low-order framework, while the systematic underprediction observed at medium and high loading remains an acknowledged model-form limitation.

https://doi.org/10.1017/aer.2026.10251 Published online by Cambridge University Press

3.0 Optimisation framework and methodology

The BEMT model validated in Section 2 was used as the objective function in the optimisation framework. The numerical solver, which is limited to forward analysis, was embedded into a two-stage metaheuristic optimisation framework to determine the best-found rotor twist geometry. In the first stage, a single-objective ABC algorithm was employed to minimise aerodynamic power consumption under a constant thrust constraint. In the second stage, the framework was extended using a multi-objective artificial bee colony (MOABC) approach [15] combined with a Pareto-based solution set to reveal the trade-off between aerodynamic performance and total blade twist.

3.1 Design variables: non-linear twist polynomial

In conventional helicopter blades, linear twist distributions are widely used because of their geometric simplicity; however, they may not provide an aerodynamically favourable twist distribution over the entire blade span under varying local dynamic-pressure conditions [2]. In the XV-15 aircraft, however, to ensure that blade sections operate at optimal angles of attack corresponding to the varying relative velocities along the radial direction, the blade twist geometry is represented using a fifth-degree polynomial as a function of the non-dimensional radial position $r = r_{\text{local}}/R$ [10].

$$\theta_{\text{twist}}(r) = p_5 r^5 + p_4 r^4 + p_3 r^3 + p_2 r^2 + p_1 r + p_0 \tag{14}$$

In Equation (14), the independent decision vector is defined as $\boldsymbol{X} = [\,p_5, p_4, p_3, p_2, p_1]$, while p_0 is determined from the reference condition $\theta_{\text{twist}}(0.75) = 0$. Since p_0 is the constant term of the polynomial, it does not affect the spanwise shape or gradient of the twist distribution, but only shifts the entire distribution uniformly. As the overall pitch level is independently adjusted through the collective-pitch trim procedure, treating p_0 as an additional independent design variable would introduce a redundant degree of freedom (DoF). Accordingly, p_0 is evaluated as

$$p_0 = -\left[p_5\,(0.75)^5 + p_4\,(0.75)^4 + p_3\,(0.75)^3 + p_2\,(0.75)^2 + p_1\,(0.75)\right] \tag{15}$$

The lower and upper bounds of the five independent polynomial coefficients were defined by applying $\pm 5\%$ variations about their corresponding reference values, with the bound ordering adjusted according to the sign of each coefficient.

3.2 Objective function: power minimisation under constant thrust

The fundamental indicator of hover performance in helicopter and tiltrotor platforms is the shaft power required to meet a specified takeoff weight. Accordingly, the objective function of the proposed optimisation algorithm is defined as the minimisation of the rotor aerodynamic power coefficient C_P.

Each candidate blade twist geometry generated from the decision variables is evaluated through the aerodynamic equilibrium condition within the BEMT solver prior to power computation. To ensure that the target thrust coefficient corresponding to the nominal DGW hover condition of the XV-15 rotor ($C_{T,\text{target}} = 0.00939$) is satisfied, the blade root pitch angle is iteratively updated until the thrust error is minimised. When the rotor disk satisfies the target thrust condition ($|\,C_T - C_{T,\text{target}}\,| \leq 1 \times 10^{-5}$), the corresponding power coefficient is computed, and the fitness function $J(X)$ is evaluated as follows:

$$J(X) = C_P(X) = \sum_{i=1}^{N} \frac{1}{2}\sigma_i \left(C_{l,i}\lambda_i + C_{d,i} r_i\right) r_i^2 \Delta r \tag{16}$$

In Equation (16), N denotes the number of blade elements along the spanwise direction [3]. The optimisation process seeks the parameter set that minimises the cost function defined in Equation (16). Minimising the power coefficient under a constant thrust condition is equivalent to maximising the aerodynamic efficiency of the rotor.

https://doi.org/10.1017/aer.2026.10251 Published online by Cambridge University Press

3.3 Artificial bee colony (ABC) algorithm setup

In the aerodynamic optimisation of the rotor blade, the ABC algorithm, a population-based metaheuristic method, was employed to handle the multidimensional search process in the design space [8, 9]. The algorithm maintains candidate designs within the prescribed aerodynamic and geometric feasibility criteria while improving the aerodynamic performance of the XV-15 rotor and is based on the collective behaviour of employed, onlooker and scout bees.

The search process is initialised with a population in which each employed bee represents a randomly generated twist polynomial. During the iterative loop, each bee generates a new candidate solution in the neighbourhood of its current position. This exploration in the continuous design space is governed by Equation (17):

$$v_{i,j} = x_{i,j} + \phi_{i,j}\left(x_{i,j} - x_{k,j}\right) \tag{17}$$

Here, k denotes a randomly selected candidate solution from the population ($k \neq i$), while $\phi_{i,j}$ is a random coefficient in the range $[-1, 1]$ that controls the magnitude of the search step. Each newly generated blade geometry is evaluated using the BEMT solver, and the resulting aerodynamic power coefficient is transformed into an inversely proportional fitness value for the selection mechanism of the algorithm:

$$fit_i = 1/\left(1 + C_{P,i}\right) \tag{18}$$

After the employed bees share the fitness values within the colony, the onlooker bees select candidate solutions based on a probabilistic selection strategy P_i.

$$P_i = \frac{fit_i}{\sum_{n=1}^{SN} fit_n} \tag{19}$$

According to Equation (19), the search process is biased toward regions with a higher probability of yielding lower power coefficients. The scout bee mechanism, on the other hand, supports the global exploration capability of the algorithm by abandoning solutions that cannot be improved within the prescribed scout limit of 300 trials.

Because of the stochastic nature of the ABC algorithm, the single-objective optimisation was performed through 30 independent runs. Each run was initialised using a different pseudo-random seed, with a colony size of 50 and a maximum budget of 10,000 number of function evaluations (NFE) per run. The solution yielding the lowest final power coefficient among the feasible solutions obtained from these independent runs was selected as the best-found solution for the subsequent aerodynamic evaluations. The stochastic repeatability of the optimisation and the consistency of the resulting twist distributions are further examined in Section 4.4.1.

The components of the search algorithm constitute the underlying framework of the multi-objective Pareto optimisation, which is presented in detail in Section 3.4.

3.4 Multi-objective optimisation (MOABC) and Pareto approach

In the second optimisation stage, total root-to-tip blade twist, $\Delta\theta = |\theta_{\text{root}} - \theta_{\text{tip}}|$, was introduced as a second objective in addition to the aerodynamic power coefficient, C_P. This geometric quantity provides a scalar representation of the overall blade-twist level, enabling a systematic examination of the trade-off between aerodynamic performance and alternative designs with lower total twist. The manufacturing-related physical basis for this choice is supported by composite-blade studies showing that root-to-tip twist and blade geometry are associated with fibre-path development during fabrication and with mould configuration [32, 34]. Nevertheless, manufacturing behaviour also depends on local variables such as surface curvature, fibre paths, steering radius and process conditions [33]; therefore, $\Delta\theta$ is used here as a geometric objective representing total blade twist rather than as a direct measure of manufacturability.

Within this framework, two design objectives are considered simultaneously. The first objective function, f_1, is the minimisation of the aerodynamic power coefficient, C_P, whereas the second objective

https://doi.org/10.1017/aer.2026.10251 Published online by Cambridge University Press

function, f_2, is the minimisation of the total root-to-tip blade twist variation, $\Delta\theta$. These conflicting objectives are transformed into a scalar cost function using the weighted sum method [13, 14]:

$$J_{total}(X) = w_1 \cdot \bar{f}_1(X) + w_2 \cdot \bar{f}_2(X) \tag{20}$$

Here, w_1 and w_2 denote the weight coefficients that vary according to design priorities ($w_1 + w_2 = 1$), and $\bar{f}_n$ represents the normalisation values that enable objectives with different orders of magnitude to be summed together. The normalisation process was performed by squeezing both objectives between 0 and 1:

$$\bar{f}_n = \frac{f_n - f_{n,min}}{f_{n,max} - f_{n,min}} \tag{21}$$

The algorithm was run by systematically varying the weighting coefficients, resulting in a Pareto front rather than a single solution. This front represents the trade-off between the aerodynamic power coefficient and total blade twist and defines the non-dominated solution set with respect to C_P and $\Delta\theta$ [13, 14].

Through this approach, the design alternatives presented in Section 4 are based on a consistent analytical framework that supports engineering decision-making.

4.0 Results and discussion

4.1 Single-objective hover performance optimisation

In the first stage of the optimisation process, a constrained single-objective ABC algorithm was employed to evaluate the aerodynamic performance potential of the XV-15 rotor blade under hover conditions. At this stage, the objective function was defined solely in terms of minimising the aerodynamic power coefficient, while total blade twist was not included as a second objective. The optimisation process focused on determining a fifth-order twist distribution that minimises the rotor power coefficient under a constant target thrust coefficient. To represent the nominal design gross weight hover condition of the XV-15, the target thrust coefficient was set to $C_{T,\text{target}} = 0.00939$. Under this operating condition, the original XV-15 reference blade evaluated using the BEMT solver yielded a power coefficient of $C_{P,\text{ref}} = 8.9049 \times 10^{-4}$ and an FOM of $FM_{\text{ref}} = 0.7223$. During the optimisation, the prescribed aerodynamic feasibility limits and geometric oscillation constraints were enforced. To suppress non-physical radial oscillations that may arise from the mathematical nature of high-order polynomials, undesirable variations in the twist distribution were restricted through a geometric penalty condition applied at the BEMT radial stations. In this way, all candidate geometries were compared under the same target thrust condition and within the same aerodynamic and geometric feasibility criteria.

Among the feasible solutions obtained from the optimisation runs, the configuration with the lowest power coefficient was identified as the best-found solution of the present study. For this geometry, $C_{P,\text{best}} = 8.1360 \times 10^{-4}$ and $FM_{\text{best}} = 0.7905$ were obtained. Compared with the reference XV-15 geometry at the same target thrust coefficient, the optimised twist distribution resulted in an approximately 8.63% reduction in power coefficient and an approximately 9.45% relative increase in FOM within the present BEMT framework.

As shown in Figure 7, the best-found twist distribution obtained by the ABC algorithm preserves the overall spanwise character of the reference XV-15 geometry while reshaping the twist distribution, particularly in the inboard and mid-span regions. For the resulting geometry, the root twist angle is approximately $\theta_{\text{root}} = 21.50°$, while the tip twist angle is approximately $\theta_{\text{tip}} = -10.94°$, yielding a total root-to-tip twist variation of approximately $\Delta\theta = 32.44°$. This value corresponds to a lower total root-to-tip twist than that of the reference geometry. However, because the single-objective optimisation was focused exclusively on reducing aerodynamic power requirement, total blade twist was not treated as an independent optimisation objective at this stage. Therefore, Section 4.2 examines how aerodynamic

https://doi.org/10.1017/aer.2026.10251 Published online by Cambridge University Press

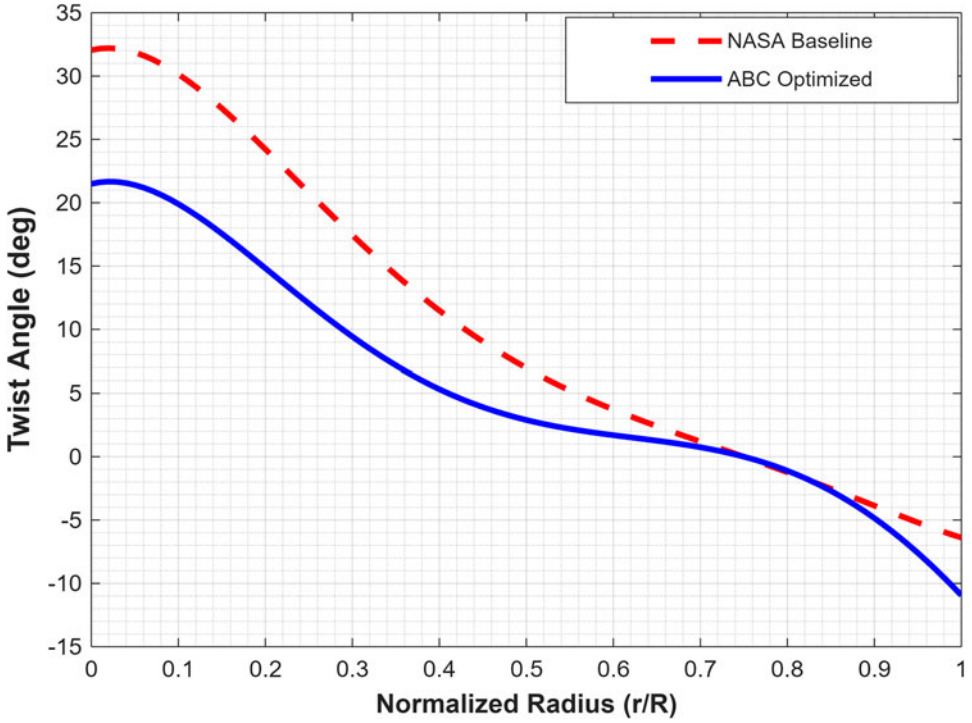


Figure 7. *Original and optimised twist distribution.*

performance changes as the design is shifted toward lower total blade-twist values within the multi-objective optimisation framework. The resulting MOABC solutions characterise the Pareto trade-off between aerodynamic performance and total blade twist.

4.2 Multi-objective analysis of aerodynamic performance and total blade twist

Although the single-objective optimisation performed in Section 4.1 successfully reduced the aerodynamic power consumption of the rotor, the trade-off between aerodynamic efficiency and total blade twist requires further evaluation. For this purpose, a MOABC approach was applied, and the relationship between the aerodynamic power coefficient and total twist variation was investigated using the solutions obtained under different weighting combinations. The resulting non-dominated solutions are presented in Figure 8.

As shown in Figure 8, the original XV-15 reference geometry has a power coefficient of approximately $C_P = 0.0008905$ and a total root-to-tip blade twist of 38.45°. The multi-objective optimisation yielded solutions with both lower power coefficients and lower total blade twist than the reference geometry, indicating that the reference design does not lie on the non-dominated boundary with respect to the two objectives considered. For Pareto solutions with greater emphasis on aerodynamic performance, the power coefficient decreases to approximately 0.000814–0.000821, while the total blade twist decreases to approximately 30.8°–32.2°. Relative to the reference geometry, these values correspond to approximately 7.8–8.6% lower power coefficient and 16.3–19.9% lower total blade twist. Toward the lower-twist region of the Pareto front, total blade twist values of approximately 20.8°–21.6° are obtained, corresponding to reductions of approximately 43.8–45.9% relative to the reference geometry; however, the power coefficient increases to approximately 0.000900–0.000907, approximately 1.1–1.9% above the reference value. These results quantitatively characterise the aerodynamic consequences associated with progressively reducing total blade twist. The percentage reductions in total twist characterise the

https://doi.org/10.1017/aer.2026.10251 Published online by Cambridge University Press

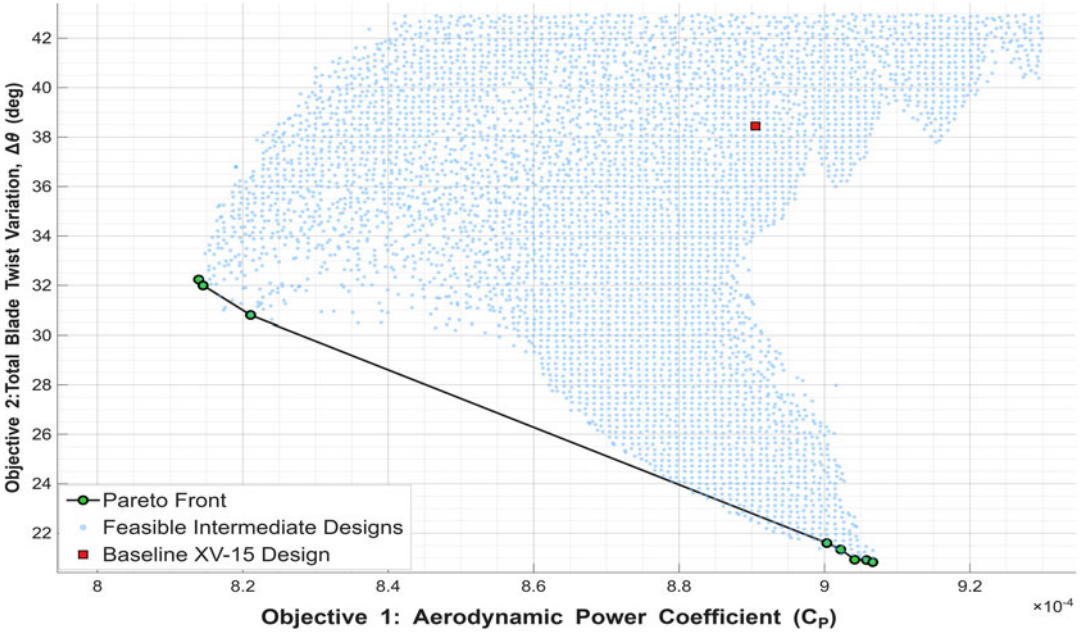


Figure 8. *Pareto front and search space for aerodynamic power coefficient and total blade twist variation.*

geometric change in the blade, while their significance from a manufacturability perspective should be assessed in the context of the local blade geometry and the specific manufacturing process.

The scattered point cloud represents a representative subset of the feasible intermediate designs evaluated during the optimisation. In the subsequent aerodynamic evaluations of this study, the solution obtained from the optimisation scenario in which aerodynamic performance is fully prioritised ($w_1 = 1, w_2 = 0$) is used as the reference. For this solution, the power coefficient was determined as $C_P = 0.0008136$, with a total twist of approximately 32.44°.

4.3 Sectional aerodynamic load and inflow distribution of the optimised blade

To examine the radial aerodynamic changes associated with the reduction in power coefficient obtained from the single-objective optimisation, the sectional angle-of-attack and induced-inflow distributions of the reference XV-15 and optimised geometries were compared. Both geometries were evaluated at the same target thrust coefficient, $C_{T,\text{target}} = 0.00939$.

As shown in Figure 9, the reference XV-15 geometry reaches relatively high angles of attack of approximately $14° - 15°$ in the inboard region, whereas the corresponding peak for the optimised geometry is reduced to approximately $9° - 10°$. The optimised twist distribution provides a more balanced and comparatively more uniform angle-of-attack distribution, particularly over the inboard and mid-span regions. The two distributions approach each other at approximately $r/R \approx 0.64$, beyond which the optimised geometry exhibits slightly higher angles of attack over the outboard region. This behaviour indicates a redistribution of the sectional aerodynamic loading along the blade. In addition, the number of radial stations exceeding the prescribed C_l limits decreases from 14 for the reference geometry to 2 for the optimised geometry.

To quantify the change in the induced-inflow distribution, the area-weighted mean, area-weighted standard deviation and coefficient of variation were employed. The area-weighted spatial formulation [16] and the use of the coefficient of variation for flow-uniformity assessment [17] were adopted for this purpose. Each BEMT station represents an annular area given by

https://doi.org/10.1017/aer.2026.10251 Published online by Cambridge University Press

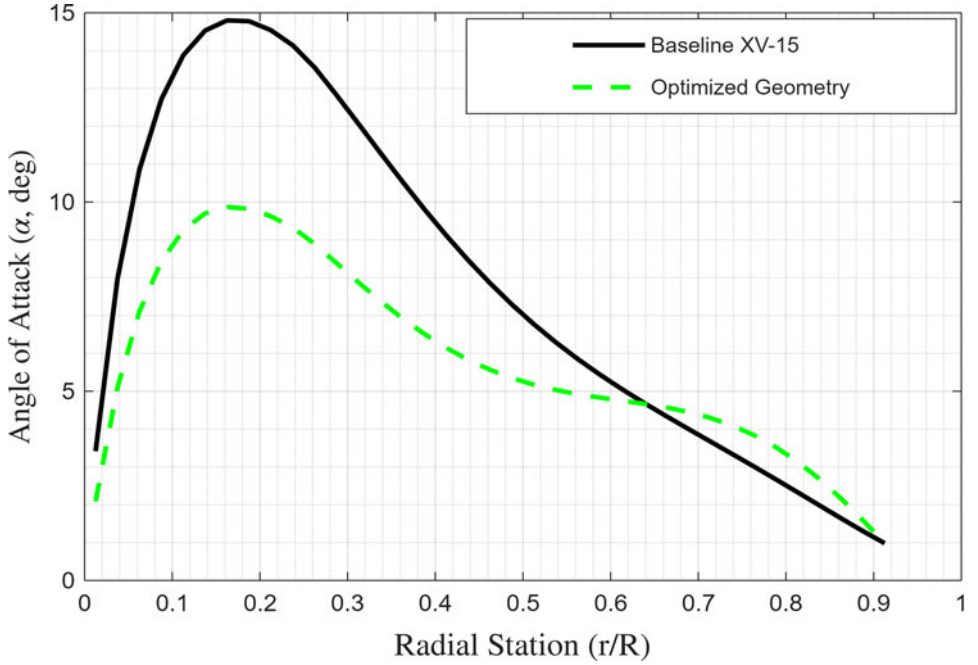


Figure 9. *Sectional angle-of-attack distribution.*

$\Delta A_k = \pi[(r_k + \frac{\Delta r}{2})^2 - (r_k - \frac{\Delta r}{2})^2] = 2\pi r_k \Delta r$. Because the common factor 2π cancels in the normalised area-weighted expressions, the area-weighted mean induced-inflow ratio is calculated as [16]

$$\overline{\lambda}_A = \frac{\sum_{k=1}^{N_s} r_k \, \lambda_k \, \Delta r}{\sum_{k=1}^{N_s} r_k \, \Delta r} \tag{22}$$

where N_S denotes the number of radial stations included in the evaluation, r_k is the non-dimensional radial position at station k, λ_k is the corresponding induced-inflow ratio and Δr is the non-dimensional radial increment.

$$E_\lambda = \sqrt{\frac{\sum_{k=1}^{N_s} r_k (\lambda_k - \overline{\lambda}_A)^2 \, \Delta r}{\sum_{k=1}^{N_s} r_k \, \Delta r}} \tag{23}$$

The coefficient of variation, which represents the relative magnitude of the inflow variation with respect to the mean inflow level, is calculated as [17]

$$CV_\lambda = 100 \, \frac{E_\lambda}{\overline{\lambda}_A} \tag{24}$$

Lower values of E_λ and CV_λ correspond to a more uniform induced-inflow distribution [16, 17].

Figure 10 shows that the optimised geometry produces a more balanced radial induced-inflow distribution. This trend is also supported by the quantitative results presented in Table 3. The area-weighted standard deviation decreases from 9.2277×10^{-3} to 7.6359×10^{-3}, corresponding to a reduction of approximately 17.25%, while the coefficient of variation decreases from 16.39% to 13.91%, corresponding to a reduction of approximately 15.14%. These results indicate that the optimised geometry provides a more uniform induced-inflow distribution than the reference XV-15 geometry [16, 17]. The association between a more uniform induced-velocity distribution and a lower induced-power requirement at constant thrust is consistent with momentum theory [2, 3]. Accordingly, the observed radial redistribution is consistent with the lower power coefficient obtained at the same target thrust coefficient.

https://doi.org/10.1017/aer.2026.10251 Published online by Cambridge University Press

Table 3. *Quantitative comparison of induced-inflow uniformity metrics*

Metric	Baseline XV-15	Optimised geometry	Change (%)
Area-weighted mean inflow, $\bar{\lambda}_A$	0.05630	0.05490	−2.49
Area-weighted standard deviation, E_λ	0.009228	0.007636	−17.25
Coefficient of variation, CV_λ	16.39%	13.91%	−15.14

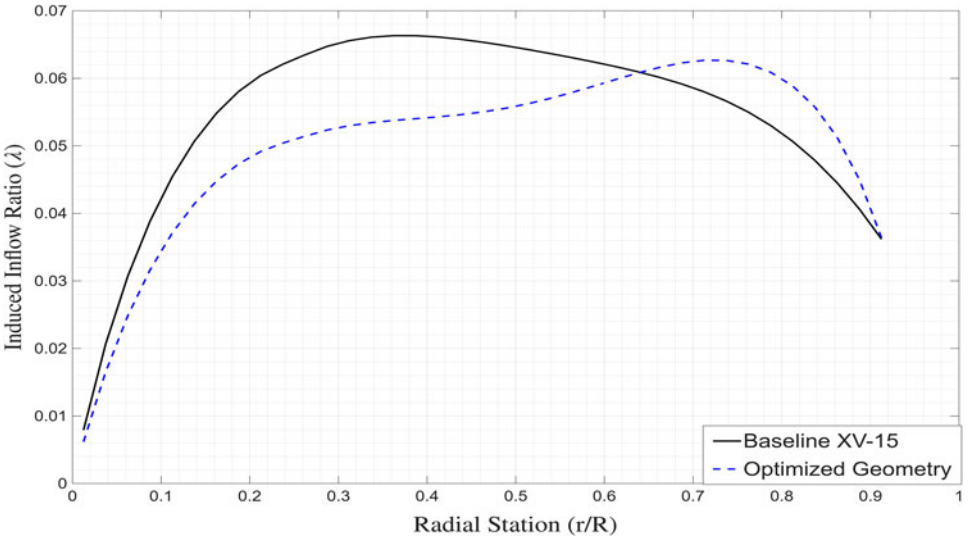


Figure 10. *Original and optimised induced inflow distribution.*

4.4 Design space and algorithm convergence characteristics

This section examines the convergence behaviour and stochastic repeatability of the optimisation process together with the aerodynamic characteristics of the design space. First, the convergence histories obtained from independent ABC runs and the consistency of the resulting blade twist distributions are evaluated. The aerodynamic performance variation within the design space is then examined using two-dimensional cross-sections defined by selected coefficient pairs of the fifth-order twist polynomial. All evaluations were performed at the same target thrust coefficient corresponding to the nominal DGW hover condition.

4.4.1 Convergence behaviour and stochastic repeatability of the ABC optimisation

Because of the stochastic nature of the ABC algorithm, assessing convergence based on a single run is insufficient to characterise the repeatability of the optimisation process. Therefore, 30 feasible runs were performed using the same optimisation settings defined in Section 3.3. The same aerodynamic and geometric feasibility criteria and penalty mechanism were applied in all runs, and each run was conducted with a maximum budget of 10,000 NFEs. In this section, the convergence histories and final objective-function values obtained from the independent runs are evaluated together to assess the stochastic repeatability of the algorithm, followed by an examination of the consistency of the resulting blade twist distributions.

Figure 11 presents the best-so-far power-coefficient histories for 30 independent ABC runs, together with the mean convergence trajectory and the ±1 SD standard-deviation band. A rapid reduction in C_P is observed during the early stage of the optimisation, accompanied by a marked narrowing of the spread among the independent runs. The inset, focusing on approximately the first 1, 500 NFE, provides a more detailed view of this early convergence behaviour. As the search progresses, further improvements in

https://doi.org/10.1017/aer.2026.10251 Published online by Cambridge University Press

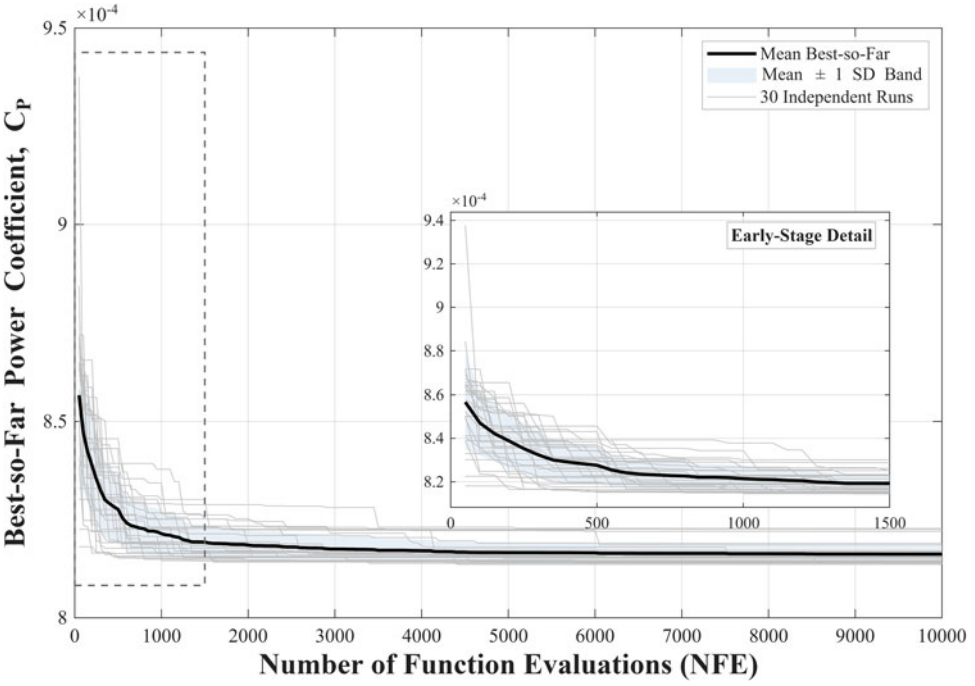


Figure 11. *Convergence behaviour across 30 independent ABC runs.*

the mean best-so-far value become progressively smaller, and the independent runs approach similarly low C_P levels. This behaviour indicates that the algorithm repeatedly reaches comparable low objective-function values despite different pseudo-random initialisations.

In addition, 27 of the 30 independent runs produced final objective-function values within 1.0% of the best-found solution, further demonstrating the repeatability of the objective-function values across the independent runs. Stochastic repeatability statistics of the 30 independent ABC runs are presented in Table 4.

Figure 12 presents the mean blade twist distribution obtained from the 30 independent runs, together with the ±1 standard-deviation band, the minimum–maximum envelope and the twist distribution of the best-found solution. The geometric variability among the runs is more pronounced in the root and inboard blade regions, while the spread progressively narrows toward the outboard region. The mean spanwise pointwise standard deviation was calculated as 0.8111°, with a maximum pointwise standard deviation of 1.6942° occurring at the blade root. In addition, the root mean square error (RMSE) of the individual run twist distributions relative to the mean twist distribution was 0.8173°. These results indicate that, although the final objective-function values are highly repeatable across the independent runs, a certain degree of geometric variability remains among twist distributions that achieve similarly low objective-function values, particularly in the inboard blade region.

The repeated convergence of the independent runs to closely clustered low objective-function values provides evidence of stochastic repeatability; however, it does not constitute a mathematical proof of global optimality. Therefore, the final configuration reported in this study is referred to as the best-found solution rather than the global optimum.

4.4.2 Examination of the design space structure and FOM distribution

Representing the blade twist distribution using a fifth-order polynomial results in a multidimensional design space defined by the polynomial coefficients. To visualise how aerodynamic performance varies

https://doi.org/10.1017/aer.2026.10251 Published online by Cambridge University Press

Table 4. *Stochastic repeatability statistics of the 30 independent ABC runs.*

Metric	Value
Feasible runs	30/30
Best-found C_P	8.1360238×10^{-4}
Mean C_P	8.1619855×10^{-4}
Standard deviation	2.4732×10^{-6}
Maximum C_P	8.2278070×10^{-4}
Range	9.1783×10^{-6}
Coefficient of variation	0.3030%

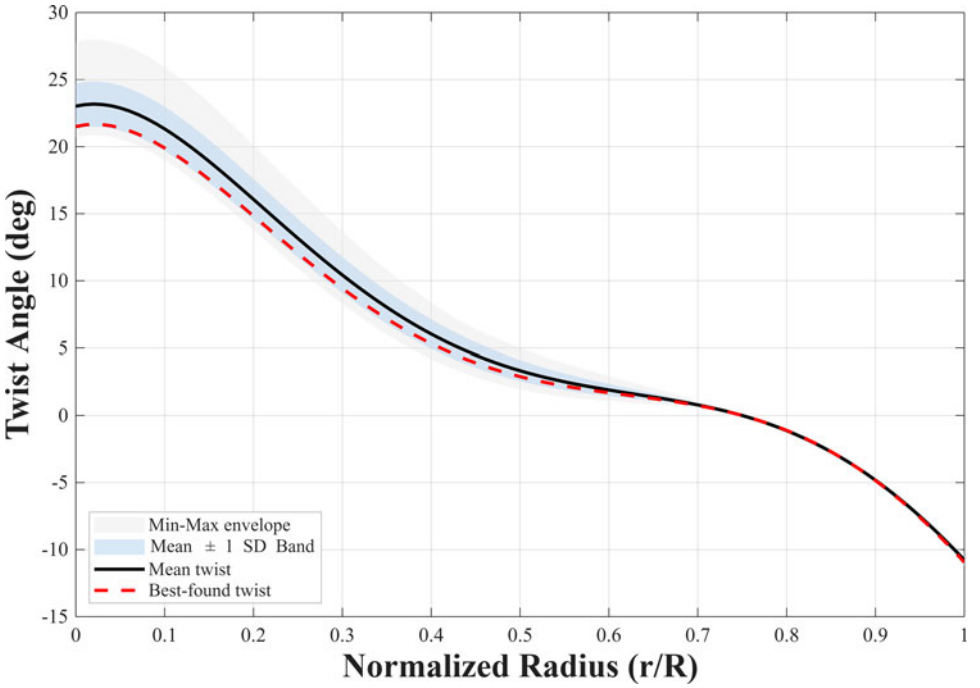


Figure 12. *Consistency of blade twist distributions across 30 independent ABC runs.*

within this space, two-dimensional cross-sections were constructed for selected coefficient pairs, and the corresponding FOM distributions were examined.

The FOM is defined as [2]:

$$FM = \frac{C_T^{3/2}}{\sqrt{2}C_P} \tag{25}$$

FM varies monotonically and inversely with the power coefficient C_P under constant-C_T conditions. Therefore, the *FM* and C_P surfaces provide equivalent aerodynamic performance rankings, and only the *FM* surfaces are presented to avoid redundant visualisation.

The two-dimensional cross-sections shown in Figures 13 and 14 indicate that the aerodynamic performance does not exhibit the same dependence on different polynomial coefficient pairs. In the p_4-p_2 plane, relatively high *FM* values are maintained over a broader and more continuous region, whereas in the p_5-p_3 plane, the high-performance region is concentrated within a narrower range. This behaviour indicates that, within the examined two-dimensional cross-sections, the aerodynamic performance exhibits different sensitivities to different coefficient combinations.

https://doi.org/10.1017/aer.2026.10251 Published online by Cambridge University Press

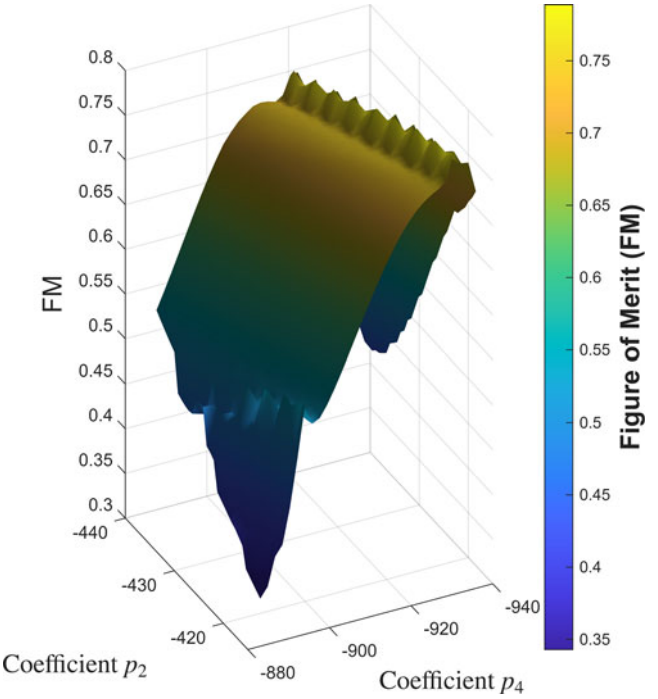


Figure 13. *FOM surface for the p4–p2 coefficient pair.*

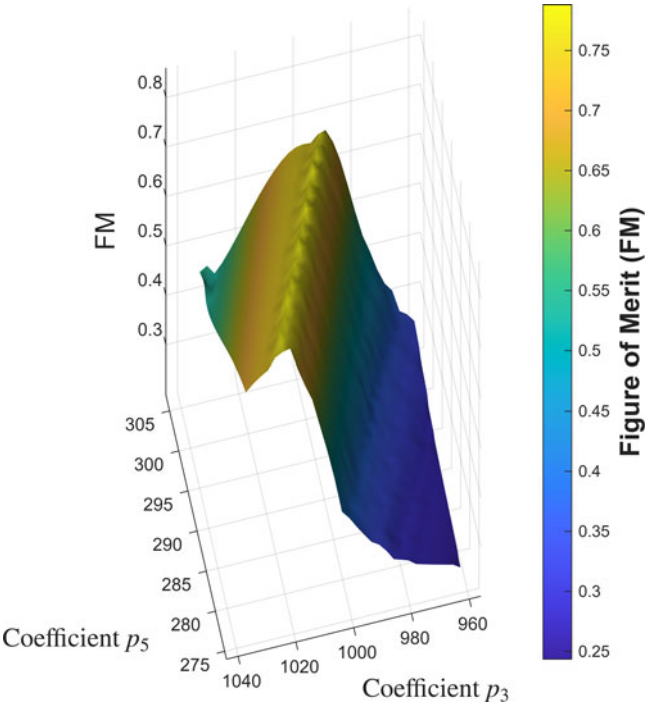


Figure 14. *FOM surface for the p5–p3 coefficient pair.*

https://doi.org/10.1017/aer.2026.10251 Published online by Cambridge University Press

Table 5. *Baseline and optimised rotor comparison*

Parameter	Baseline(NASA XV-15)	Optimised(ABC)	Change (%)
Thrust coefficient (C_T)	0.00939	0.00939	0.00
Power coefficient (C_P)	0.0008905	0.0008136	−8.63
Figure of merit (FOM)	0.7223	0.7905	+ 9.45
Root twist angle (θ_{root})	32.057°	21.50°	−32.94
Tip twist angle (θ_{tip})	−6.388°	−10.94°	+ 71.26
Total blade twist variation ($\Delta\theta$)	38.45°	32.44°	−15.63
Polynomial coeff. (p_5)	289.98	286.2730	−1.28
Polynomial coeff. (p_4)	−892.87	−931.2661	+ 4.30
Polynomial coeff. (p_3)	987.06	1012.7958	+ 2.61
Polynomial coeff. (p_2)	−438.31	−416.7201	−4.93
Polynomial coeff. (p_1)	15.695	16.4797	+ 5.00
Polynomial coeff. (p_0)	32.057	21.4965	−32.94

The surfaces presented here represent selected two-dimensional cross-sections of the multidimensional design space. They should therefore be interpreted as complementary analyses of how interactions between the selected coefficient pairs influence the aerodynamic performance distribution, rather than as a complete representation of the entire design space. Within the examined cross-sections, high *FM* values are not distributed uniformly but are concentrated around specific coefficient combinations. These surfaces consequently provide additional insight into the local structure of the aerodynamic performance landscape associated with the optimisation problem.

5.0 Conclusions and future work

This study investigated the effect of blade twist geometry on the hover performance of the XV-15 tiltrotor. The results reported here are specific to the XV-15 configuration, the nominal hover operating condition considered, and the present BEMT-based modelling framework. Within this scope, the blade twist distribution was found to have a significant influence on the rotor power requirement and aerodynamic efficiency. The effect of the optimised twist geometry on rotor performance is evaluated comparatively with the reference (NASA XV-15) geometry in Table 5.

Table 5 shows that the best-found twist geometry provides improved predicted aerodynamic performance relative to the reference XV-15 geometry under the same nominal DGW hover thrust condition within the present BEMT framework.

The multi-objective analysis revealed a clear Pareto trade-off between aerodynamic performance and total blade twist. For Pareto solutions prioritising aerodynamic performance, the total blade twist was reduced by approximately 16–20% relative to the reference XV-15 geometry while maintaining a lower power coefficient. Further reductions in total blade twist were accompanied by an increase in power requirement. Thus, the second optimisation stage quantitatively characterised the aerodynamic consequences associated with moving toward lower total blade-twist levels.

Within the scope of future work, the present optimisation framework may be extended to other flight regimes. Accordingly, incorporating forward flight conditions and the asymmetric load distribution that arises depending on the advance ratio into the optimisation will make it possible to expand the model to encompass more realistic flight scenarios.

Additionally, when the computational efficiency provided by the BEMT-based approach and the high accuracy offered by CFD-based analyses are evaluated together, hybrid approaches where these two methods are coupled constitute a significant research direction for future studies.

Acknowledgements. This study was supported by Turkish Aerospace Industries under the Lift Up Project (Award Number: 689f3df12daca). The authors gratefully acknowledge Turkish Aerospace Industries for its financial and technical support.

https://doi.org/10.1017/aer.2026.10251 Published online by Cambridge University Press

References

[1] Adkins, C.N. and Liebeck, R.H. Design of optimum propellers, *J. Propul. Power*, 1994, **10**, pp 676–682.
[2] Leishman, J.G. *Principles of Helicopter Aerodynamics*, Cambridge University Press, 2nd ed., 2006, Cambridge, UK.
[3] Johnson, W. *Rotorcraft Aeromechanics*, Cambridge University Press, 2013, Cambridge, UK.
[4] Seddon, J. and Newman, S. *Basic Helicopter Aerodynamics, 3rd ed.*, John Wiley & Sons, 2011, Chichester, UK.
[5] Glauert, H. Airplane Propellers, in Durand, W.F. (Ed), *Aerodynamic Theory*, Springer, 1935, Berlin, Heidelberg, pp 169–360.
[6] Johnson, C.S. and Barakos, G.N. A framework for optimising aspects of rotor blades, *The Aeronaut. J.*, 2011, **115**, pp 147–161.
[7] Vu, N.A., Lee, J.W., Le, T.P.N. and Nguyen, S.T. A fully automated framework for helicopter rotor blades design and analysis including aerodynamics, structure, and manufacturing, *Chin. J. Aeronaut.*, 2016, **29**, pp 1610–1626.
[8] Karaboga, D. An idea based on honey bee swarm for numerical optimization, Technical Report TR06, Erciyes University, Engineering Faculty, Computer Engineering Department, Kayseri, Türkiye, 2005.
[9] Karaboga, D. and Basturk, B. A powerful and efficient algorithm for numerical function optimization: artificial bee colony (ABC) algorithm, *J. Glob. Optim.*, 2007, **39**, pp 459–471.
[10] Harris, F.D. *Hover Performance of Isolated Proprotors and Propellers-Experimental Data, NASA Ames Research Center, Moffett Field, CA, NASA/CR-2017-219486, Dec* 2017.
[11] Prouty, R.W. *Helicopter Performance, Stability, and Control*, Krieger Publishing Company, 2002, Malabar, FL.
[12] Anderson, J.D. Jr. *Fundamentals of Aerodynamics, 5th ed.*, McGraw-Hill, 2011, New York, NY, USA.
[13] Gunantara, N. A review of multi-objective optimization: methods and its applications, *Cogent Eng.*, 2018, **5**, pp 1502242.
[14] Marler, R.T. and Arora, J.S. Survey of multi-objective optimization methods for engineering, *Struct. Multidisc. Optim.*, 2004, **26**, pp 369–395.
[15] Akbari, R., Hedayatzadeh, R., Ziarati, K. and Hassanizadeh, B. A multi-objective artificial bee colony algorithm, *Expert Syst. Appl.*, 2012, **39**, pp 64–74.
[16] Ianniruberto, I., Astori, D., Saitta, S., Milesi, D., Calle, P.V., Gaudino, M., Girardi, L.N., Humphrey, J.D., Weinsaft, J.W., Votta, E. and Redaelli, A. From case studies to cohort of patients: automating FSI simulations to uncover downstream effects of ascending aortic grafts, *Ann. Biomed. Eng.*, 2026. https://doi.org/10.1007/s10439-026-04313-4.
[17] Abattouy, I., Meslem, A., Mahdaoui, M., Ahachad, M., Guillard, C., Dappozze, F., Randrianasolo, T., Peruchon, L., Brochier, C. and Lamaa, L. Modeling and optimization of a tangential photocatalytic reactor for uniform distribution of pollutant-laden air on the reactive area, *Chem. Eng. J.*, 2026, **534**, p 174695. https://doi.org/10.1016/j.cej.2026.174695.
[18] Marr, R.L. *Wind Tunnel Test Results of 25 Foot Tilt Rotor During Autorotation, Bell Helicopter Co., Fort Worth, TX, NASA-CR-137824, Feb.* 1976.
[19] Zeng, L., Hu, J., Pan, D. and Shao, X. Automated design optimization of a mono tiltrotor in hovering and cruising states, *Energies*, 2020, **13**(5), p 1155. https://doi.org/10.3390/en13051155.
[20] Lim, J.W., Allen, L.D., Haehnel, R.B. and Dettwiller, I.D. An Examination of Aerodynamic and Structural Loads for a Rotor Blade Optimized with Multi-Objective Genetic Algorithm, in Vertical Flight Society 77th Annual Forum & Technology Display, Virtual, May 10–14, 2021. https://doi.org/10.4050/F-0077-2021-16770
[21] Wilke, G., Bailly, J., Kimura, K. and Tanabe, Y. JAXA-ONERA-DLR cooperation: results from rotor optimization in hover, *CEAS Aeronaut. J.*, 2022, **13**, pp 313–333. https://doi.org/10.1007/s13272-022-00580-8.
[22] Wang, Z., Yang, Y., Zhao, H. and Wang, X. Aerodynamic optimization design of tiltrotor under multiple flight conditions, *Acta Aeronaut. et Astronaut. Sinica*, 2024, **45**(9). https://doi.org/10.7527/S1000-6893.2023.29024
[23] Shahjahan, S., Gong, A., Moore, A. and Verstraete, D. Optimisation of proprotors for tilt-wing eVTOL aircraft, *Aerosp. Sci. Technol.*, 2024, **144**. https://doi.org/10.1016/j.ast.2023.108835.
[24] Ding, Z., Zhang, C., Peng, M. and Li, J. A reformulated-vortex-particle-method-based aerodynamic multi-objective design optimization strategy for proprotor in hover and high-altitude cruise, *Aerospace*, 2024, **11**(11), p 906. https://doi.org/10.3390/aerospace11110906.
[25] Sancak, T. The Effect of Twist Distribution on Rotor Performance and Its Applications on Rotor Blades, M.Sc. thesis, Graduate School, Istanbul Technical University, Istanbul, Türkiye, 2025.
[26] Kang, D.H., Park, N.E., Cho, J.D. and Park, S.H. Study on proprotor airfoil optimization for improving aerodynamic performance of tiltrotor aircraft, part II: evaluation of proprotor performance, *Journal of Computational Fluids Engineering*, 2025, **30**, pp 56–67. https://doi.org/10.6112/kscfe.2025.30.2.056.
[27] Dayhoum, A., Ramirez-Serrano, A. and Martinuzzi, R.J. Performance optimization of shrouded rotors: fixed vs. Variable pitch in hover and forward flight, *Appl. Sci.*, 2025, **15**(17), p 9594. https://doi.org/10.3390/app15179594.
[28] Park, S., Lee, J., Choi, J., Kang, Y.-E., Hong, Y., Wilke, G. and Yee, K. Aerodynamic Optimization for Rotor Blade with Structural Design in Hover and Forward Flight, in *Vertical Flight Society 81st Annual Forum & Technology Display*, May 20–23, 2025, Virginia Beach, VA, USA. https://doi.org/10.4050/F-0081-2025-0070
[29] Thurman, C.S. and Wang, L. Multifidelity Multipoint Proprotor Blade Optimization for Urban Air Mobility, in *Vertical Flight Society 81st Annual Forum & Technology Display*, May 20–23, 2025, Virginia Beach, VA, USA. https://doi.org/10.4050/F-0081-2025-0069
[30] Woodgate, M.A. and Barakos, G.N. High fidelity CFD/CSD method for rotor blade optimization, *Aerosp. Sci. Technol.*, 2026, **174**, p. 111895. https://doi.org/10.1016/j.ast.2026.111895
[31] Gadekar, R.D.Abhishek and Kothari, M. Design Optimization of a Rotor Blade for a Variable Pitch Quadrotor Unmanned Air Vehicle, in *AHS International 74th Annual Forum & Technology Display*, May 14–17, 2018, Phoenix, AZ, USA. https://doi.org/10.4050/F-0074-2018-12722

https://doi.org/10.1017/aer.2026.10251 Published online by Cambridge University Press

[32] Ho-Nguyen-Tan, T., Hong, G., Jaiswal, A.P., Oh, Y., Bae, K.J., Yu, J., Kim, M. and Yoon, S.H. Fiber distortion impact on the bending deformation of laminated fan blade structures: a numerical and experimental study, *Composites Part B: Engineering*, 2025, **305**, p 112670. https://doi.org/10.1016/j.compositesb.2025.112670.

[33] Bakhshi, N. and Hojjati, M. An experimental and simulative study on the defects appeared during tow steering in automated fiber placement, *Compos. Part A: Appl. Sci. Manuf.*, 2018, **113**, pp 122–131. https://doi.org/10.1016/j.compositesa.2018.07.031

[34] Torpan, R. and Zaharia, S.-M. Manufacturing process of helicopter tail rotor blades from composite materials using 3D-printed moulds, *Appl. Sci.*, 2024, **14**, p 972. https://doi.org/10.3390/app14030972

Cite this article: Pekacar H., Güneş G., Baysaltan İ.D., Çağlar A. and Bilgic H.H. BEMT-based blade twist optimisation of a tiltrotor in hover using artificial bee colony algorithm. *The Aeronautical Journal*, https://doi.org/10.1017/aer.2026.10251

https://doi.org/10.1017/aer.2026.10251 Published online by Cambridge University Press